μSR investigation of magnetism in κ-(ET)$_2X$: Antiferromagnetism

B. M. Huddart,[1] T. Lancaster,[1] S. J. Blundell,[2] Z. Guguchia,[3] H. Taniguchi,[4] S. J. Clark,[1] and F. L. Pratt[5,*]

[1]*Department of Physics, Centre for Materials Physics, Durham University, Durham DH1 3LE, United Kingdom*
[2]*Oxford Physics, Clarendon Laboratory, Parks Road, Oxford OX1 3PU, United Kingdom*
[3]*Laboratory for Muon Spin Spectroscopy, Paul Scherrer Institut, CH-5232 Villigen PSI, Switzerland*
[4]*Graduate School of Science and Engineering, Saitama University, Saitama 338-8570, Japan*
[5]*ISIS Neutron and Muon Source, STFC-RAL, Chilton, Didcot OX11 0QX, United Kingdom*

(Received 18 August 2022; revised 10 November 2022; accepted 16 November 2022; published 13 January 2023)

We study magnetism in the κ-(ET)$_2X$ family of charge-transfer salts using implanted muon spectroscopy in conjunction with detailed *ab initio* electronic structure calculations using density functional theory (DFT). ET stands for the electron donor molecule bis(ethylendithio)tetrathiafulvalene and X is an anion. The DFT calculations are used to establish molecular spin distributions, muon stopping sites, and dipolar field parameters, that allow us to make a quantitative interpretation of the experimental results. Materials in the κ-(ET)$_2X$ family with $X = Ag_2(CN)_3$ and $X = Cu_2(CN)_3$ have attracted particular interest, as they have the attributes of quantum spin liquids, showing no magnetic ordering down to 30 mK in zero field μSR and in NMR, despite having exchange couplings of order 200–250 K. In contrast, the material with $X = Cu[N(CN)_2]Cl$ has an antiferromagnetic (AF) ordering transition with T_N in the region of 23–30 K. In order to better understand the muon spectroscopy signature of magnetism in this whole family of compounds at both low and high magnetic fields, we look in detail at the case $X = Cu[N(CN)_2]Cl$. As the first step in our study, the spin density distribution for the ET dimer is calculated using DFT and used to simulate the 3.7 T ^{1}H-NMR spectrum of this salt, with the spectrum showing good agreement with that measured previously [K. Miyagawa, A. Kawamoto, Y. Nakazawa, and K. Kanoda, Phys. Rev. Lett. **75**, 1174 (1995)]. Best match to the data is found for antiferromagnetic interlayer ordering and an ordered moment per dimer of 0.25 μ_B. DFT is also used to explore muon stopping sites for this salt, finding one set of sites resulting from muonium addition to C=C double bonds in the ET layer, with muons stopping in the anion layer forming another group of sites. The dipolar fields associated with each of the stopping sites is computed and these are compared with the precession frequencies observed in the ZF-μSR spectrum [M. Ito, T. Uehara, H. Taniguchi, K. Satoh, Y. Ishii, and I. Watanabe, J. Phys. Soc. Jpn. **84**, 053703 (2015)]. Best match to the ZF-μSR spectrum is obtained with the mode of interlayer ordering having FM character and an ordered moment per dimer of 0.31 μ_B for muon sites in the anion layer and 0.36 μ_B for muonium sites in the ET layer. New measurements of TF-μSR spectra for fields up to 8 T are reported and analyzed to obtain the best estimate of the magnetic order parameter under different measurement conditions, allowing us to observe the variation of T_N with applied field and the field-induced transverse canting of the moments.

DOI: 10.1103/PhysRevResearch.5.013015

I. INTRODUCTION

Almost half a century ago, metallic conductivity was reported in the charge-transfer salt (TTF)(TCNQ) [1]. As the first example of a metallic organic conductor, this discovery proved a turning point for the field [2], with hundreds of organic conductors reported in the subsequent decades, among which over a hundred also exhibit superconductivity [3]. One of the key points of these low-dimensional organic systems is that they can be tuned across rich phase diagrams with small chemical modifications and modest hydrostatic or uniaxial pressures. Superconductivity exists on the border of ordered states in the charge and spin sectors, in common with electron-doped cuprates [4]. There is also significant evidence for the exotic Fulde-Ferrell-Larkin-Ovchinnikov (FFLO) superconducting state at high magnetic fields [5,6]. Furthermore, when the degree of geometrical frustration is sufficiently high and the system is close to the insulator to metal transition of the Mott insulator, a quantum spin liquid (QSL) state can be realized [7].

The organic molecule BEDT-TTF, commonly abbreviated as ET, is bis(ethylenedithio)tetrathiafulvalene. It forms a family of quasi-two-dimensional organic charge transfer salts, κ-(ET)$_2$X, that represent model systems for the study of Mott physics. This is because the relative strength of electron kinetic energy and Coulomb interaction can be tuned with pressure (or chemical pressure), which results in a variety of phases due to the competition between the itineracy and

*francis.pratt@stfc.ac.uk

Published by the American Physical Society under the terms of the Creative Commons Attribution 4.0 International license. Further distribution of this work must maintain attribution to the author(s) and the published article's title, journal citation, and DOI.

TABLE I. Comparison of the structural properties of three members of the κ-$(ET)_2X$ family, with the final two columns noting the space group (SG) and ground state (GS). The interlayer axis is marked by the asterisk. The structural properties were determined at 100 K for κ-Cl [15], at 13 K for κ-Ag [18], and at 5 K for κ-Cu [19].

Name	Anion X	a (Å)	b (Å)	c (Å)	β (°)	SG	GS
κ-Cl	$Cu[N(CN)_2]Cl$	12.89	29.58*	8.42	90	*Pnma*	AF
κ-Ag	$Ag_2(CN)_3$	14.95*	8.65	13.18	91	$P2_1/c$	QSL
κ-Cu	$Cu_2(CN)_3$	15.92*	8.55	13.27	114	$P2_1/c$	QSL

localization of electrons [8]. For κ-$(ET)_2X$, the coupling between face-to-face ET molecules within each dimer is strong enough that the system can be effectively described by the Hubbard model on an anisotropic triangular lattice of dimers [9]. For monovalent anions X^-, one electron is transferred from each dimer $(ET)_2$ to each anion formula unit, so that the bare system is a half-filled metal before taking into account the Hubbard repulsion, which, if sufficiently strong, can turn it into a Mott insulator.

The structural properties of the three κ-$(ET)_2X$ salts covered in our studies are listed in Table I and illustrated in Fig. 1. The ground state of this system depends on the ratio between the nearest neighbor transfer t and the second-nearest neighbor transfer t' [see Fig. 1(b)] as well as the Hubbard repulsion energy for double occupancy U. The anisotropy ratio $r = t'/t$ depends on the anion X^-, the substitution of which acts as a chemical pressure that allows one to explore the phase diagram of a Mott insulator. When $r \sim 1$ and t/U is below 0.1, a noncollinear antiferromagnetic (AF) ordered state with three sublattices at 120° to each other is expected [10]. A QSL state can however be stabilized around $r \sim 1$ when t/U is between 0.1 and 0.14 [10,11]. This is believed to be the case for κ-Cu (Table I). When r is significantly smaller than 1, the frustration is reduced and a collinear Néel AF state is expected [12]. This is believed to be the case for κ-Cl (Table I). Estimates of r for κ-Cl range from 0.44 [13] and 0.52 [14] using DFT to 0.72 using extended Hückel (EH) theory [15]. The κ-Ag salt is estimated to lie in between the κ-Cu and κ-Cl cases, with r reduced from 1, but r is not low enough to lead to the AF ordered Néel state and it remains in the QSL phase.

Muon spin rotation spectroscopy of implanted positive muons (μSR) [16] has emerged as a useful tool to study magnetism and superconductivity in many different types of organic materials [17]. These μSR measurements are highly sensitive to magnetic order, even when the magnitude of the moments is strongly suppressed by quantum fluctuations. Since the QSL phases arise from suppression of magnetically ordered phases, any partial recovery of such magnetism by perturbations such as local defects and applied magnetic fields may be detectable by the local muon probe. The principle of the muon spectroscopy technique is that the implanted muon is spin polarized and undergoes radioactive decay after a mean lifetime of 2.2 μs, producing a decay positron that can be detected by a muon spectrometer. Since the orientational distribution of the positron emission reflects the direction of the muon spin when it decays, the time dependence of the muon

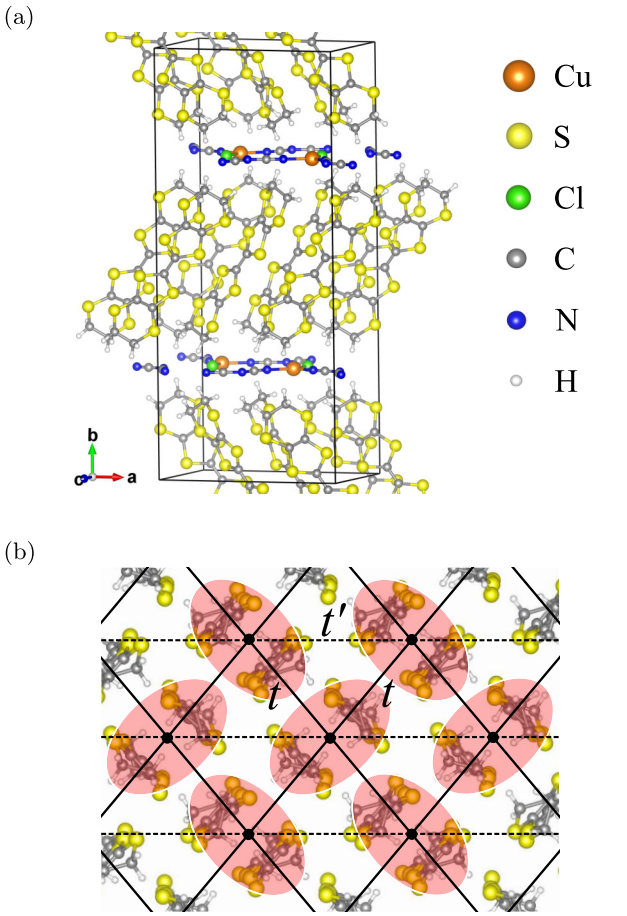

FIG. 1. (a) The structure of κ-$(ET)_2Cu[N(CN)_2]Cl$ containing two ET layers in the unit cell. (b) Crystal structure of an ET layer in κ-$(ET)_2X$ viewed along the long axis of the ET molecules. ET dimers form an anisotropic triangular lattice characterized by interdimer transfer integrals t and t'.

spin polarization can be measured via the positrons. The muon spin polarization evolves according to the local magnetic field it experiences and this field depends on the stopping site of the muon in relation to the sources of magnetism in the sample. Consequently, gaining a knowledge of the distribution of muon stopping sites in a target material is an important part of the quantitative analysis of muon spectroscopy data and this is a strong focus of the present study. These results will provide the foundation for a more detailed analysis and interpretation of the properties of the QSL members of the family, where field-induced magnetic states have been observed in the μSR data [20].

The rest of this paper is organized as follows. Section II presents analysis using DFT calculations to model the distribution of the spin density in the κ-phase ET salts and provide information about the muon stopping sites. Comparison is made with previous ^{1}H-NMR and ZF-μSR data for the AF ordered state in κ-Cl salt in order to test and validate the modeling approach. Section III presents new μSR results for κ-Cl measured under transverse magnetic fields ranging up to 8 T. Section IV discusses the main findings and conclusions of our detailed study of κ-Cl.

TABLE II. Spin distribution over the ET molecule within the molecular dimer structure of the three salts studied here for a moment of 1 μ_B on the dimer. The distribution is calculated for GAUSSIAN DFT (B3LYP/cc-pVTZ) (columns headed G) and also, for comparison in the case of κ-Cl, using CASTEP plane-wave DFT (PBE/600 eV) (column headed PW). The numbers are expressed in units of 10^{-3} of the total moment per dimer. Atomic site labels are shown in Fig. 2. Rows are listed by equivalent sites in the dimer with the names in brackets being the original labeling used in the crystal structure file. The last column shows for comparison the spin density obtained from the HOMO coefficients of a single planar ET molecule with D_{2h} symmetry and charge +0.5, based on EH theory [27].

	κ-Cl				Monomer
Site	PW	G	κ-Ag G	κ-Cu G	EH
C1	48	51	53 (C2)	52	29
C2	32	27	29 (C1)	25	29
C3	24	22	19 (C6)	18 (C4)	13
C4	22	20	22 (C5)	16 (C3)	13
C5	24	21	17 (C4)	21 (C6)	13
C6	20	20	24 (C3)	29 (C5)	13
C7	0	0	0 (C10)	1 (C8)	0
C8	0	0	0 (C9)	0 (C7)	0
C9	2	1	0 (C8)	0 (C10)	0
C10	1	−1	1 (C7)	1 (C9)	0
S1	70	76	78 (S4)	74 (S2)	84
S2	76	83	79 (S3)	71 (S1)	84
S3	66	72	66 (S2)	74 (S4)	84
S4	63	68	76 (S1)	74 (S3)	84
S5	10	8	8 (S8)	6 (S6)	14
S6	11	8	8 (S7)	6 (S5)	14
S7	12	9	13 (S6)	14 (S8)	14
S8	17	15	7 (S5)	18 (S7)	14

II. SPIN DISTRIBUTION AND MUON SITES

A. Spin density distribution over the ET dimer

In order to calculate internal fields in magnetic phases we need to know the distribution of magnetic moment across the molecular dimers. As noted above, these systems can be phenomenologically described by models treating the dimers as $S = 1/2$ spins within the Hubbard model on an anisotropic triangular lattice at half-filling [9]. However, such a model ignores the possibility of an active intradimer degree of freedom, which recently has been found to be important in some cases [21–23]. Moreover, a simple model of a spin centered on a dimer is likely to be insufficient when considering local probe techniques such as μSR that are sensitive to the magnetic field (and hence spin density) at specific positions within the structure.

The analysis of previous studies of κ-Cl using local probe techniques also required knowledge of spin density distributions for the ET dimer. In the ^{1}H-NMR study by Miyagawa *et al.* [24], the highest occupied molecular orbital (HOMO) coefficients of an EH calculation for spin densities were used. In the μSR study by Ito *et al.* [25], 0.5 μ_B per dimer was assumed to be distributed across the atoms as a set of point dipoles with the magnitude of the moment on each atom depending on the square of the EH HOMO coefficient on a monomer [26,27] (Table II).

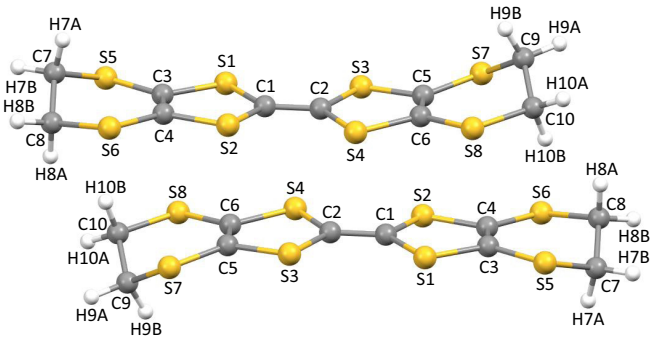

FIG. 2. Atomic site labels for the ET dimer. The two molecules in the dimer are related by inversion symmetry.

Here, we calculate the spin density distribution across the ET dimer (with a charge +1) using the Gaussian orbital DFT code GAUSSIAN [28]. We use the B3LYP functional [29,30] and the triple-zeta cc-pVTZ basis set [31]. It is also possible to do a similar calculation using CASTEP plane-wave DFT with an expanded lattice of widely separated dimers and an example of the result for κ-Cl is provided for comparison, giving a very similar distribution. The results of the spin distribution calculations for isolated dimers taken from the low temperature crystal structures of κ-Cl, κ-Ag, and κ-Cu are shown in Table II. The site labeling is shown in Fig. 2. The spin densities shown in Table II are derived from a Mulliken population analysis. The spin density is mainly distributed over the central TTF core consisting of C1-C6 and S1-S4. This suggests that the rough assumption of a spin-1/2 hole located at the center of the dimer is a reasonable first approximation, but we note that the extended nature of the spin density distribution will be important when considering the magnetic field experienced by muons close to the ET dimers or by H atoms on the molecule.

B. Testing the spin distribution via the AF ordered state

Study of the reference AF state in κ-Cl allows us to check the accuracy of the DFT calculated spin distribution over the dimer and gain some understanding of the muon states and their coupling to the magnetism in this type of structure. The atomic spin distribution used to calculate dipolar fields is the product of the individual dimer distribution and the modulation of the overall dimer spin associated with the magnetic ordering. Besides giving a thorough test of the model for magnetic order in κ-Cl, this analysis will also provide us with a sound basis for interpreting the field-induced magnetic states in κ-Ag and κ-Cu, that will be the focus of a subsequent paper.

Firstly, we calculate the ^{1}H-NMR spectrum on the basis of the dipolar fields at the H sites and compare it with published data, allowing a basic check of the spin distribution over the dimer, the mode of magnetic ordering and the size of the ordered moment. Secondly, we calculate the most stable muon stopping sites for this system using the DFT+μ method. From knowledge of these sites and the original dimer spin distribution we predict the dipolar fields at these sites and hence the ZF precession spectra to test against the published μSR results. Finally in Sec. III we present and interpret the new high field TF-μSR data, testing against models for the

magnetic state in κ-Cl and revealing a significant increase in the AF ordering temperature with magnetic field applied perpendicular to the layers.

1. The nature of the AF state in κ-Cl

A transition to the AF ordered state was first detected as an anomaly at $T_N = 27$ K in the ^{1}H-NMR spin-lattice relaxation rate $1/T_1$ [24]. The NMR spectra displayed splitting into a number of distinct lines corresponding to a discrete distribution of local fields, thus implying a magnetic structure that is commensurate with the lattice. However, the assignment of the magnetic easy axis in κ-Cl has proven controversial. While the magnetic phase of this material was initially described in terms of a spin-density wave with weak ferromagnetism [32], it is now recognized that the localized spins on the dimers are aligned antiferromagnetically within the layers with a small canting [24]. However, the precise spin orientations in the zero-field ordered state have remained unclear, since techniques such as magnetization, NMR and torque measurements can only suggest *possible* spin structures at low fields. Magnetic neutron diffraction can provide definitive information about spin structures in many materials, but the weak and highly delocalized nature of the spins in the ET salts has made such studies impractical.

The presence of a weak ferromagnetic (FM) moment in addition to the AF order was initially established by magnetization measurements [24], which showed an enhanced susceptibility when the field is applied parallel to the conducting layers. These measurements also displayed an abrupt jump at $T = 23$ K when the field was applied perpendicular to the layers. This is usually an indication of a spin-flop transition that would result for easy axis parallel to the field and therefore suggested that the magnetic easy axis is perpendicular to the conducting layers, i.e., the b axis. The identification of the b axis as the magnetic easy axis was backed up by magnetic anisotropy measurements for field orientations close to the b axis [33], which also demonstrated that the spins cant away from this axis by an angle of 0.06°, such that a small resultant FM moment lies along the c axis. This study also highlighted the importance of the Dzyaloshinskii-Moriya (DM) interaction [34,35] on the magnetic properties of κ-Cl. Experimental characterization of the DM vectors in κ-Cl was achieved by carrying out ^{13}C NMR measurements while sweeping the direction of the external field [36].

A zero-field spin structure was recently proposed by Ishikawa *et al.* [37], that is significantly different to those proposed in past studies. This structure was deduced by examining spin reorientations for fields applied along each of the crystallographic axes. These results, taken together with the knowledge of the DM vectors, backed up by DFT calculations [38], and the high-field spin structures from NMR [36,39] allowed Ishikawa *et. al*. to conclude that the magnetic easy axis is in fact the c axis, with the net canting moment parallel to the a axis. In this model the transition for field perpendicular to the layers that takes place around 0.4 T at 5 K [37] is regarded as a spin-flop transition of the canting moments in successive layers, produced by a switch of the interlayer ordering mode from FM at low fields to AF at fields above the spin-flop transition.

TABLE III. Magnitude of the local dipolar field components along the b axis for the eight H sites in the magnetically ordered state of κ-Cl, given for the two possible modes of interlayer coupling. The field values are expressed in terms of the ordered moment per dimer.

Site	Position (cell fraction)	AF interlayer mT/μ_B	FM interlayer mT/μ_B
H7A	(0.452, −0.142, 0.219)	7.81	7.69
H7B	(0.462, −0.172, 0.061)	1.36	1.24
H8A	(0.278, −0.184, 0.070)	1.93	2.02
H8B	(0.340, −0.207, 0.216)	1.22	0.74
H9A	(−0.107, 0.211, 0.164)	2.29	1.74
H9B	(−0.042, 0.184, 0.297)	3.44	3.12
H10A	(−0.227, 0.172, 0.311)	2.34	2.54
H10B	(−0.221, 0.147, 0.142)	7.24	7.13

2. Dipolar fields at the H sites and comparison with NMR

To test the accuracy of the spin density distribution that we obtained, we use it to simulate the ^{1}H-NMR spectrum of κ-Cl and compare this to the spectra measured by Miyagawa *et al.* [24]. The frequency shift of the signal for each ^{1}H in this experimental geometry is proportional to the b component of the local field at the ^{1}H position. We therefore calculate these dipolar field components at each of the ^{1}H positions in κ-Cl (Table III). The spin density at each of the atoms in the ET dimer is represented by a point dipole centered on the atom with the magnitude of the moment proportional to the spin density that we calculated and with direction pointing along the c axis (we can safely neglect the small FM canting, which is not significant for a local probe technique). All dipolar fields in this paper are calculated using the program DipoleCalc [40]. Note that we only consider the moments on C1-C6 and S1-S8 and neglect the very small spin density on the C atoms of the terminal ethylene groups (C7-C10). Adjacent dimers are AF coupled within the layers and we examined the alternative scenarios of AF or FM coupling between the c axis moments in successive layers.

The NMR intensity $I(\nu)$ is calculated from the fields listed in Table III as a sum of Lorentzians resulting from each of the eight distinct ^{1}H atomic sites, i.e.,

$$I(\nu) = \sum_{i=1}^{8} \left[\frac{0.5}{1 + \left(\frac{\nu - \nu_i}{w}\right)^2} + \frac{0.5}{1 + \left(\frac{\nu + \nu_i}{w}\right)^2} \right], \qquad (1)$$

where the Lorentzians are centered on $\pm\nu_i = \pm\gamma_H B_{b,i}$, with $B_{b,i}$ the b- component of the dipolar field at the H atom i and γ_H the ^{1}H gyromagnetic ratio. (We consider both positive and negative fields as the AF structure means that for each H atom experiencing a field B_i there will be a crystallographically equivalent H atom in an adjacent cell experiencing a field $-B_i$.) We use the width $w = 6$ kHz to aid comparison with the experimentally measured spectra.

The resultant simulated spectra are shown in Figs. 3(a) and 3(b) and consist of eight pairs of symmetrically split peaks, which form four relatively well separated spectral bands. The experimental ^{1}H-NMR spectra are shown in Fig. 3(c) [24] for comparison, both well above and well below the transition. Below the transition the spectrum is split into three strong bands and one much weaker band, with the splitting becoming

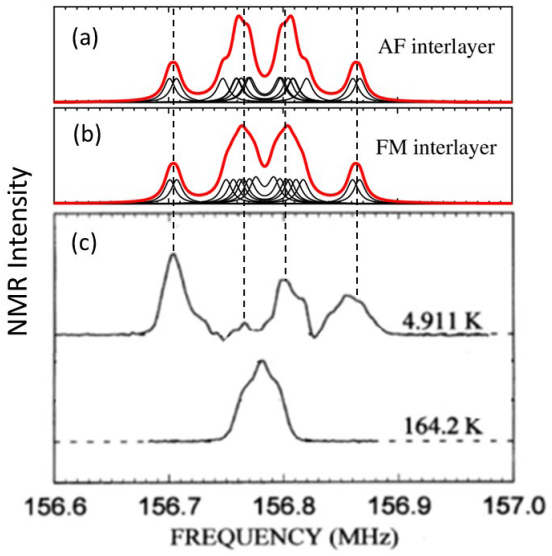

FIG. 3. [(a), (b)] The predicted ^{1}H-NMR spectra in the AF ordered phase of κ-Cl for magnetic field of 3.7 T along the b axis, based on the spin distribution calculated using GAUSSIAN (Table II), scaled to a moment of 0.25 μ_B per dimer. (c) The measured ^{1}H-NMR spectra for a field of 3.7 T along the b axis reported by Miyagawa *et al.* [24]. Spectra are shown for the AF phase well below T_N and for the paramagnetic phase well above T_N.

larger as the temperature is lowered. The splitting of the spectra into a finite number of lines is evidence for commensurate AF order below 27 K. The overall splitting from the center is ±80 kHz, corresponding to maximum fields of order 2 mT at the ^{1}H sites. In our simulated spectra, the fields are calculated by scaling to this overall splitting, giving a moment of 0.25 μ_B per dimer, which provides the best match to the measured overall splitting of the spectrum for both AF and FM modes of interlayer coupling (Fig. 3). This ordered moment based on the DFT spin distribution is lower than the broad range of 0.4–1.0 μ_B per dimer that was previously estimated using a molecular spin distribution derived from EH theory [24]. Our obtained moment of 0.25 μ_B is also significantly lower that the value ∼0.6 μ_B expected for the $S = 1/2$ Néel antiferromagnet on a square lattice [41], which corresponds to the effective regime expected from the DFT derived estimates of around 0.5 for r [13,14]. This indicates that r is actually closer to the phase boundary between the Néel and QSL states than the DFT calculations would suggest. The ordered moment size is further discussed in relation to the phase diagram and the muon results in Sec. II B 9.

Although the measured low-temperature spectrum in Fig. 3(c) is not symmetrical, showing some unexpected intensity modulation, the spectral features are clear enough to compare with the predicted spectra. The AF interlayer mode was recently suggested to be present for b axis fields above the spin-flop transition at 0.4 T [37]. Since the NMR was measured at 3.7 T, it will be in the high field region above this transition. From the line shape of the inner bands, we note that the measured NMR spectrum appears to be a little closer to the simulation for the case of AF interlayer order rather than FM interlayer order, which would be in agreement with the conclusion about the high field region from the earlier study [37].

In the measured spectrum some additional shoulders are observable on the inner side of the outer peaks that are not present in the predicted spectra. One possible origin for this could be disorder in the ethylene group conformation. Frozen disorder between eclipsed and staggered ethylene group conformations can be produced below a glass transition taking place around 75 K, unless special care is taken to cool slowly through this point. Such disorder could lead to further small splittings in the experimental spectra and account for the extra shoulders. It is anyway clear from our analysis that the ^{1}H-NMR spectra in the magnetically ordered state should be very sensitive to changes in the H positions that might be induced by disorder.

3. Calculation of muon stopping sites

Besides determining the spin distributions, DFT methods can also be used to calculate possible stopping sites for an implanted muon in a computational technique known as DFT+μ. This has recently been applied successfully to a variety of materials, including many with molecular constituents, such as spin chains [42], spin ladders [43], and molecular magnets [44]. Muon stopping sites in κ-Cl were calculated here using DFT+μ with the plane-wave basis set electronic structure code CASTEP [45] and the PBE functional [46]. A cut-off energy of 490 eV was used for the plane wave basis set, resulting in pseudopotentials that converge to around 0.1 eV/atom and a 1×1×2 Monkhorst-Pack grid was used for Brillouin zone sampling [47]. van der Waals dispersion corrections were incorporated using the Tkatchenko-Scheffler method [48]. While van der Waals forces have been previously shown to have little effect on the structure of κ-Cl, they have a large effect on the computed unit cell parameters in κ-Ag and κ-Cu [49] and have thus been included to ensure consistency with our subsequent calculations on these materials.

Muons, represented by an ultrasoft hydrogen pseudopotential were placed in a unit cell of κ-Cl and the resulting structures relaxed until the forces on the atoms were all $<5\times10^{-2}$ eV/Å and the total energy and atomic positions converged to 2×10^{-5} eV and 1×10^{-3} Å respectively. Both charged (+1) and neutral simulation cells were studied. The charged cell case corresponds to adding a bare positive muon, whereas the neutral cell case represents the addition of muonium, i.e., a muon plus an electron. One hundred fourteen initial muon sites were sampled using Poisson disk sampling with a minimum separation of 2 Å between initial muon positions [50]. Structural relaxations of the original atoms plus implanted muon yielded a large number of crystallographically distinct muon stopping sites, with the sites being associated with both the organic dimers and the anion layers. Similar sites are obtained for both charged and uncharged cells.

4. Molecular sites

We consider first the muon sites associated with the ET dimers, corresponding to neutral muonium (Mu^0) addition. The lowest energy sites obtained in our calculations involve an unphysical bond breaking between the terminal C atoms

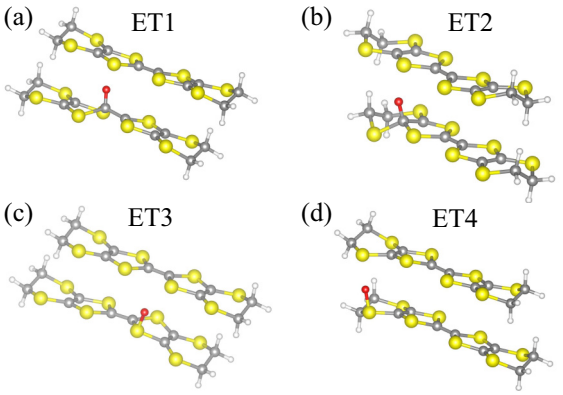

FIG. 4. The four classes of neutral muon state (Mu^0) associated with the ET dimer. Muonium addition to (a) inner and (b) outer carbon double bonds and addition to (c) inner and (d) outer sulfur atoms. Muons are shown in red. Sites are found with muons located on the inside faces of the dimer (as shown here) and also with muons located on the outside faces of the dimers. The ET3 and ET4 sulfur sites have significantly higher energy than the ET1 and ET2 carbon sites.

and the S atoms and have therefore been discarded. We find four other distinct classes of stopping site, which we illustrate in Fig. 4. We see that the muon either bonds to one of the unsaturated C atoms in the central C=C, C1 or C2 (ET1) or an outer C=C, C3-C6 (ET2) or to one of the electronegative S atoms at inner sites (ET3) or outer sites (ET4), as could be expected on chemical grounds. As found in previous studies of muon stopping sites on molecular compounds [43], the complex potential energy landscape can make establishing a hierarchy of sites in terms of increasing energy difficult. This is the case here, with sites of the type ET1 and ET2 having similar energies that span a range of around 0.3 eV. However, we do note a trend that the lowest energy sites involving bonding to S atoms (ET3 and ET4) are around 0.85 eV higher in energy than the lowest energy sites involving bonding to C atoms (ET1 and ET2). We consequently only consider molecular sites of the more stable ET1 and ET2 classes in the analysis that follows.

5. Anion layer sites

We also identify sites where the muon occupies the anion layer and report these sites as A1 to A7 in Fig. 5. The relative energies of these sites (compared to the ET sites) for charged and uncharged cells suggest that the anion layer is a more favorable stopping location for μ^+ (equivalently labeled Mu^+) than for neutral muonium (Mu^0), which would also be expected from an electrostatic argument. We therefore use site geometries from charged cells for the anion layer sites (representing Mu^+ addition), in contrast to the site geometries obtained from neutral cells that are being used for the ET sites (representing Mu^0 addition).

6. Comparison with the ZF-μSR spectrum

We now compute the dipolar fields associated with each of the muon stopping sites described in the previous section and compare these with the oscillation frequencies observed in

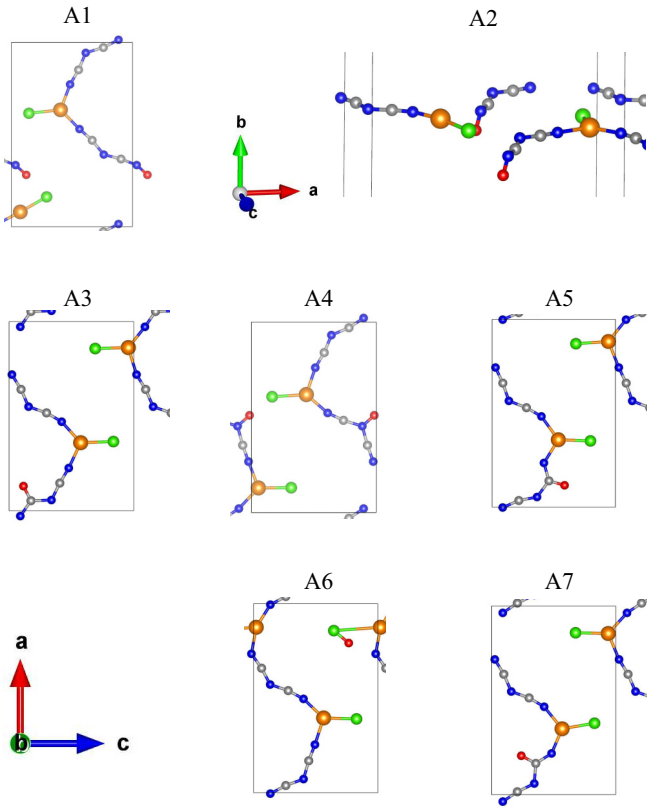

FIG. 5. Charged muon sites A1 to A7 obtained for Mu^+ stopping in the anion layer.

the ZF-μSR measurements of Ito *et al.* [25]. These μSR measurements were performed on a polycrystalline array of κ-Cl crystals at the RIKEN-RAL muon facility. Distinct muon precession frequencies were observed for $T < 21.4$ K indicating the presence of long-range magnetic order. Below T_N, the asymmetry contains two precessing components whose frequencies vary in fixed proportion to each other as a function of temperature, $\omega_1 = 0.734\omega_2$. The relative spectral weightings of the two components, $p_1 = 0.168$ and $p_2 = 0.066$ imply that the higher frequency site is occupied by a greater fraction of the muons. Fits of the temperature dependence of the muon precession frequencies to a critical fluctuation model gave an extrapolated zero-temperature field of 5.84(4) mT corresponding to ω_1. In summary, these results suggested the existence of two primary magnetically distinct muon stopping sites in κ-Cl, experiencing local magnetic fields of magnitude 5.84 mT and 4.29 mT in the ordered phase. Further analysis of the relaxation signal both by direct fitting and by a maximum entropy method (labelled here as MaxEnt) [16,51] suggests there are some low field components between 0 and 1 mT [Fig. 6(a)] in addition to the two higher field components reported previously. Labeling of these spectral components is indicated in Fig. 6(a). All data analysis was carried out using the Wimda program [52].

In order to generate the full field distribution seen by the muon we must consider all of the crystallographically (and hence magnetically) distinct sites within each class of stopping site. For example, ET1 comprises two distinct sites depending on whether the muon bonds to C1 or C2 (as

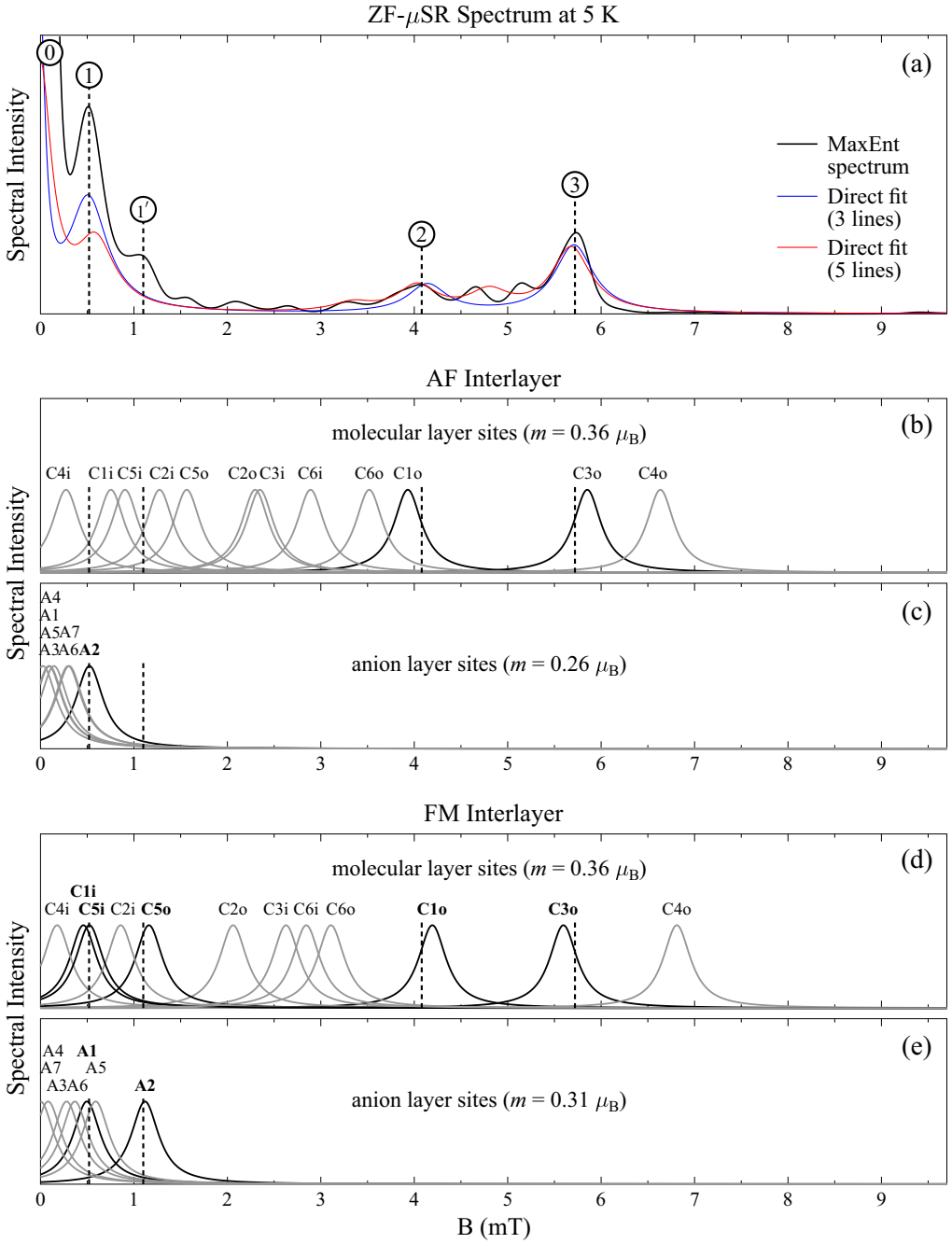

FIG. 6. (a) The experimental ZF-μSR spectrum at 5 K derived from the data of Ito *et al.* [25], obtained here from both the MaxEnt method and from direct time domain fitting of multiple precession components. Dashed lines indicate the main features used for comparison with calculated spectral components. [(b)–(e)] The calculated spectral components based on dipolar fields at the muon sites listed in Table IV. Calculated site spectral components that can be assigned to measured spectral features are indicated in bold. These spectral component sets are obtained with best-matched moments of 0.36 μ_B per dimer for the molecular layers and lower moments for the anion layers. [(b), (c)] The AF mode of interplanar ordering and [(d), (e)] the FM mode of interlayer ordering. The FM mode provides the optimal overall match to the main spectral features in the data, with assignment being made to seven of the lowest energy muon stopping sites (see Table IV).

labeled in Fig. 2). Sites with the muon bonded to each of the distinct atoms within the ET molecule are taken from the set of relaxed muon positions. In cases where the required site was not obtained from the structural relaxations, new sites were generated by applying a quasimirror plane of the ET molecule to a representative position within the same class. The resulting muon positions are then relaxed within the full structure to ensure that they are stable within the crystal. In the case of the ET sites, we posit the formation of a local singlet state on the occupied dimer via a muonium addition process in which the extra electron introduced by the muonium pairs up with the existing electron from the radical dimer. Thus when calculating the corresponding dipolar field we "turn off" the spin density on the dimer to which the muon has added to

TABLE IV. The muon stopping sites in κ-Cl. The upper section shows the ET1 and ET2 molecular stopping sites and the lower section lists the A1–A7 anion stopping sites. For each site the relative energy within the group is given. The molecular site label suffixes i and o respectively refer to sites on the inner and outer faces of the ET molecules within the dimer. Dipolar fields $B_{\rm dip}$ with FM and AF modes of interlayer ordering are shown for comparison with ZF-μSR data. The third column shows assignment to the main features in the ZF spectrum (Fig. 6) based on FM interlayer ordering. The last three columns show dipolar field components along the b axis for comparison with the TF-μSR data. The final column shows the local field response to a field-induced bulk magnetization along the b axis. N' is given by $(3N-1)/2$, where N is the demagnetization factor. For the platelet geometry of the experiment we take $N=1$ and thus $N'=1$. In that case, it can be seen that there is close cancellation between the two terms of ΔB_b for all of the anion sites, leading to an expectation of no significant overall shift of their average peak positions with field.

Mu state	Site	ZF peak (FM)	Position (cell fraction)	$E_{\rm rel}$ (meV)	$B_{\rm dip}$(FM) (mT/$\mu_{\rm B}$)	$B_{\rm dip}$(AF) (mT/$\mu_{\rm B}$)	$\lvert B_b\rvert$ (FM) (mT/$\mu_{\rm B}$)	$\lvert B_b\rvert$ (AF) (mT/$\mu_{\rm B}$)	ΔB_b ($M \parallel b$) (mT/$\mu_{\rm B}$)
Mu^0	C6i		(0.153, −0.068, −0.143)	0	7.99	8.05	0.10	0.12	$-12.7-9.6N'$
	C1i	1	(0.086, −0.044, 0.020)	0	1.29	2.10	0.29	0.29	$-10.0-9.6N'$
	C3o	3	(0.361, −0.059, 0.219)	15	15.72	16.30	5.17	5.17	$-6.1-9.6N'$
	C5i	1	(0.063, −0.111, 0.015)	31	1.47	2.52	0.29	0.27	$-4.8-9.6N'$
	C1o	2	(0.225 0.000, 0.253)	36	11.78	10.95	3.94	3.94	$-15.2-9.6N$
	C5o	1′	(0.079, 0.120, 0.225)	67	3.26	4.36	0.83	0.77	$-2.6-9.6N'$
	C2o		(0.147, 0.047, 0.258)	92	5.79	6.40	1.24	1.25	$-8.3-9.6N'$
	C4o		(0.278, −0.067, 0.339)	196	19.13	18.48	15.30	15.31	$-11.5-9.6N'$
	C4i		(0.145, −0.121, 0.095)	205	0.50	0.76	0.15	0.11	$-4.4-9.6N'$
	C3i		(0.203, −0.094, −0.046)	224	7.38	6.54	1.57	1.57	$-9.7-9.6N'$
	C2i		(0.004, 0.005, 0.021)	325	2.41	3.55	0.35	0.35	$-9.9-9.6N'$
	C6o		(−0.018, 0.099, 0.365)	333	8.73	9.80	3.42	3.38	$-7.9-9.6N'$
Mu^+	A1	1	(0.281, 0.249, 0.123)	0	1.58	0.34	0.09	0.23	$9.4-9.6N'$
	A2	1′	(0.031, 0.216, 0.975)	131	3.56	2.00	1.29	1.30	$11.8-9.6N'$
	A3		(0.370, 0.250, 0.615)	151	0.89	0.55	0.45	0.51	$10.1-9.6N'$
	A4		(0.010, 0.250, 0.515)	191	0.26	0.10	0.15	0.10	$8.8-9.6N'$
	A5		(0.383, 0.251, 0.087)	336	1.88	0.37	0.49	0.25	$9.0-9.6N'$
	A6		(0.208, 0.250, 0.234)	414	1.17	1.13	0.45	1.04	$9.7-9.6N'$
	A7		(0.294, 0.250, 0.740)	442	1.69	1.17	0.28	1.08	$9.7-9.6N'$

reflect this local electronic singlet state. The rationale behind this assumption will be discussed later, but here we note that neglecting to do so results in dipolar fields of several tens of mT at the ET sites, which are an order of magnitude larger than those observed experimentally. The Mu^0 sites on the ET molecules are labeled via the C site number and a suffix i or o indicating whether the site is on an inner or an outer face of the ET molecule within the dimer.

Calculating the dipolar field at each magnetically distinct muon stopping site allows us to simulate the magnetic field distribution experienced by the muon. The dipolar fields for the lowest energy muon stopping sites are listed in Table IV. For spectral simulation, the intensity contribution I_i from each site i to the ZF-μSR spectrum is represented by a Lorentzian centered on the local field B_i at that site, i.e.,

$$I_i(B) \propto \frac{\sin^2\theta_i}{1+[(B-B_i)/w]^2}, \tag{2}$$

where θ_i is the angle between the local field and the initial muon polarization and w is a characteristic spectral width. For a polycrystalline powder sample, the angular dependence is averaged out and the numerator of Eq. (2) becomes 1.

From Table IV it can be seen that site C4o provides the largest dipolar field, however it has a relatively high energy compared to other stopping sites. The next strongest dipolar fields are for sites C3o and C1o. These can be assigned respectively to spectral peaks 3 and 2. This immediately sets the scale of the ordered moment to be 0.36 $\mu_{\rm B}$ per dimer for the Mu^0 sites in the ET layer in both cases of AF [Fig. 6(b)] and FM [Fig. 6(d)] interlayer coupling. The positions of the spectral contributions from the other ET sites follow on from fixing this moment and the results are shown in Figs. 6(b) and 6(d). In the case of AF interlayer ordering, the low field sites do not match particularly well to the low-field spectral features. On the other hand, for the FM mode of interlayer ordering, a good match to all the spectral features is obtained by just considering the low energy stopping sites, C1i, C5i, C5o, C3o, and C1o, as flagged in column 3 of Table IV. The only one out of the six lowest energy Mu^0 sites that does not appear to contribute significantly to the measured spectrum is C6i. The increased moment compared to that deduced from the ^{1}H-NMR can be regarded as the effect of introducing a nonmagnetic spin vacancy defect on the triangular spin lattice by forming the singlet state on the dimer containing the addition site. This will produce a local decrease in the frustration and recover part of the moment.

In the case of the anion layer sites, the perturbation effect of the muon is expected to be smaller than for the ET layer sites, since one is only introducing a charge defect into the nonmagnetic layer rather than inserting a spin vacancy defect into the magnetic layer. Hence a moment value intermediate between 0.25 and 0.36 $\mu_{\rm B}$ would be expected for the anion sites. In the case of AF interlayer coupling, a match of site A2 to spectral peak 1 can be obtained with a moment of 0.26 $\mu_{\rm B}$ [Fig. 6(c)], which is only slightly perturbed from the

bare moment value obtained from the NMR analysis. With the FM mode of interlayer coupling, we find that the two lowest energy anion sites A1 and A2 can reproduce spectral peaks 1 and 1′ with a moment of 0.31 μ_B [Fig. 6(e)]. Our overall conclusion here is that the FM mode of interlayer ordering provides the best match to the strongest features in the ZF-μSR data. From our combined analysis of the previous ^{1}H-NMR and ZF-μSR results we can also confirm that the data are consistent with an ordered moment with its easy spin direction lying along the c axis. The spin transition occurring around 0.4 T for field along b is also confirmed to be consistent with a transition between the FM and AF modes of interlayer ordering in the presence of a weak canted moment.

7. Singlet formation

An important feature of our analysis, absent in the previous study [25], is taking into account the formation of singlet state on the host ET dimer for sites involving the muonium forming a bond with one of the atoms in an ET molecule. This phenomenon is incorporated in our calculations by "turning off" the spins on the dimer that is occupied by the muon. A large part of the evidence for such a mechanism being at play is the unfeasibly large dipolar fields that result when this procedure is not carried out (they are up to several tens of mT and thus an order of magnitude larger than those observed experimentally). However, this behavior also has strong physical motivation. When muonium brings an extra electronic spin into an isolated dimer, there are only two possible states that can be formed: a singlet or a triplet; the singlet is found to have significantly lower energy in DFT calculations using GAUSSIAN [28]. A similar phenomenon was observed for the organic ferromagnets p-NPNN [53] and F4BImNN [44], where muonium addition to oxygen atoms within the nitronyl nitroxide group gives rise to a local electronic singlet.

8. Comparison with ALC studies

Sites associated with the ET dimer obtained from our first principles calculations can be compared with those suggested by μSR measurements on the ET molecule using the technique of avoided level crossing (ALC) [54,55]. Crystals comprising only ET donor molecules are insulators as there are no acceptor molecules to facilitate charge transfer. Hence, when muonium reacts with one of the molecules, the muonium electron remains localized on the molecule forming a muoniated radical species and this can be studied using ALC spectroscopy [56]. The ALC spectra of ET exhibit two strong broad resonances at 0.85 T and 1.05 T, corresponding to isotropic hyperfine coupling constants of around 230 MHz and 280 MHz [57]. These are likely to be associated with muonium addition to the inner and outer C=C bonds, respectively, i.e., ET1 and ET2 sites in our present classification [57,58]. Our present results therefore indicate that the same muonium addition sites are present in the negatively charged ET dimer as in the neutral ET molecule, thus providing a consistent picture of the stopping sites present in different ET-based materials.

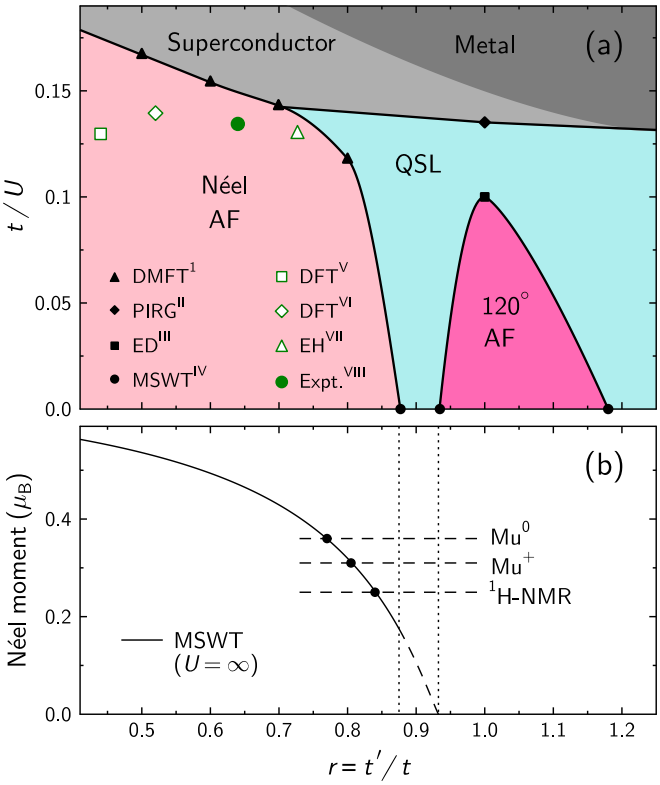

FIG. 7. (a) Phase diagram for the anisotropic triangular lattice extended Hubbard model. Open green symbols are derived from calculated values of t and t' for κ-Cl, taking a U value of 0.5 eV. The solid-green symbol is derived from experimental Shubnikov de Haas (SdH) data. The references for this panel are (I) dynamical mean field theory (DMFT) study of Kyung and Tremblay [12], (II) path integral renomalization group (PIRG) study of Yoshioka *et al.* [11], (III) exact diagonalization (ED) study of Yang *et al.* [10] and (IV) modified spin wave theory (MSWT) study of Hauke [61], (V) DFT study of Kandpal *et al.* [13], (VI) DFT study of Koretsune and Hotta [14], (VII) EH study of Hiramatsu *et al.* [15], (VIII) experimental estimate obtained by extrapolating the SdH data of Yamauchi *et al.* [62] to zero pressure [63]. (b) The ordered moment calculated from MSWT in the Heisenberg limit [61] compared with the values obtained from our analysis of NMR and μSR data.

9. The magnitude of the ordered moment

We next consider the absolute values of ordered moment obtained in experiment versus that expected for the anisotropic lattice extended Hubbard model with the parameters previously calculated for κ-Cl. This is illustrated in Fig. 7(a), which shows a phase diagram based on a number of different theoretical studies. Calculated values for r range from the smaller values of 0.44 [13] and 0.52 [14] obtained from DFT methods to the larger value of 0.73 obtained from the EH method [15]. Estimates of U from these calculations are generally based on unreliable approximations, so we use a U value of 0.5 eV for the plot, which is broadly consistent with the infrared spectrum [59,60] and with κ-Cl being in the Néel AF phase rather than the superconducting phase.

We already noted in Sec. II B 2 that the moment obtained for the NMR data is significantly lower than that expected for the square lattice limit of the Néel phase in the anisotropic

triangular lattice Heisenberg AF. The ordered moment in the Néel AF phase depends most strongly on how close one is to the phase boundary with the QSL phase and this is illustrated in Fig. 7(b) using the moment derived from modified spin wave theory in the limit $t/U \to 0$ [61]. This calculated moment extrapolates to zero at $r = 0.93$, which is the quantum critical point (QCP) for the onset of the noncolinear magnetic phase. The moments derived from our analysis of the H atom probe sites in ^{1}H-NMR and the Mu^+ and Mu^0 probe sites from our μSR results are indicated as horizontal dashed lines in Fig. 7(b), which allows us to estimate the bare r ratio of κ-Cl and also provide some quantification of the perturbing effect of the muon in its different charge states. From the ^{1}H-NMR moment of 0.25 μ_B a value of 0.84 can be estimated for r, which is 0.09 below the QCP. This is an upper limit, since the moment reduction due to having a finite t/U has not been taken into account. Including a moment reduction factor for finite t/U of the order seen in DMRG calculations [12] would give a slightly lower estimate of 0.8, which is 0.13 below the QCP. The presence of the muon locally reduces the frustration and increases the ordered moment giving the effect of a charge or spin defect, which could be regarded as a sort of local "chemical pressure". From Fig. 7(b) it can be seen that the local shift in r with respect to the unperturbed NMR point is of order -0.035 for the Mu^+ charged anion site and -0.07 for the singlet-forming Mu^0 ET site.

10. Estimation of r from SdH data

An experimental estimate of r can be derived from analyzing the SdH data of κ-Cl in its pressure induced metallic state [62] using the approach previously used for κ-Cu [63]. Linear extrapolation of the α pocket Fermi surface area to zero pressure gives an area that is 14.6% of the Brillouin zone. Comparison with the r dependence of this area for the κ-Cl structure gives the value $r = 0.64$, which lies in between the larger one of the two DFT estimates [14] and the EH estimate [15]. This is plotted as the solid green symbol in Fig. 7(a), taking its t/U value as the average of the other estimates on either side. At this t/U value, the QCP marking the boundary with the QSL phase is at $r = 0.75$. Hence the obtained r value is 0.11 below this QCP, which is similar to the displacement of 0.13 that we estimated from the size of the unperturbed moment compared with the MSWT calculations [Fig. 7(b)]. Compared to the values derived from experiment, the underestimation of r by DFT and overestimation of r by EH appears to be a notable general feature of calculations for the κ-ET family [63].

C. Conclusion on muon sites and spin distribution

This section has used DFT methods to make detailed analysis of previously reported data. From the present paper building on previous studies, we are able to confirm the magnetic state in κ-Cl and the nature of its field-induced spin transitions. The parameters determined for κ-Cl on the basis of its ordered moment place it close to the phase boundary with the QSL phase and we have been able to quantify the local perturbation effect of the the presence of the muon in this frustrated spin system by close comparison between the μSR and NMR results. The insight gained in this study can be readily extended to the interpretation of μSR studies on other ET-based organic conductors, of which there have already been many [20,25,64–67].

The methodology developed here will help us to interpret the results of μSR measurements made on the quantum spin liquids κ-Ag and κ-Cu, which will be reported in a subsequent paper. The next part of the present paper concerns the TF-μSR measurements we have made on κ-Cl and their interpretation in the light of the information we have obtained in this section about the nature of the muon stopping sites and the magnetic structure.

III. TF-μSR RESULTS AT HIGH FIELD

A. Experimental details

For the high transverse field μSR measurements reported here, fully deuterated samples of κ-(d8-ET)$_2$Cu[N(CN)$_2$]Cl were prepared. Deuteration is helpful in reducing the signal broadening from nuclear dipole moments. The identical magnetization behavior between deuterated and nondeuterated samples indicates the same spin structure for each. A mosaic of crystal platelets was mounted in the muon beam at the HAL9500 instrument at the SμS facility of the Paul Scherrer Institute. The applied field was parallel to the crystal b axis and a flow cryostat was used to vary the sample temperature between 3 K and 100 K. An active veto system was used to ensure that only positron decays resulting from muons stopping in the sample were collected by the data acquisition system. The maximum entropy method [16] (MaxEnt) was used for extracting the spectral distribution of internal fields in the collected data.

B. Experimental results

1. High field

Measurements made in the HAL9500 spectrometer under high TF of 6 T and 8 T are shown in Fig. 8. The distribution of spectral intensity in the TF rotation signal is plotted versus ΔB, which is the deviation of the internal field from the applied field. A major feature of these high field spectra is that the main spectral region is split into two peaks labeled I and II. At temperatures above T_N the relative intensity of these two peaks varies with T [Figs. 8(a) and 8(d)]. The behavior changes significantly on entering the magnetic phase below T_N [Figs. 8(b) and 8(e)]. In this region peak II changes in amplitude, width and position versus T, whereas peak I remains essentially independent of T. In addition, significant satellite features appear above and below the main peaks. It was found that the most straightforward way to characterize the evolution of the new spectral features is to follow the integrated area on the wings of the spectrum that reflects the satellite features. The spectral regions used for this are marked in gray in Figs. 8(b) and 8(e). The area obtained in this way is shown in Figs. 8(c) and 8(f) and clearly reveals an increase in intensity at low T that can be used to derive the value of T_N in each case by fitting the area $A(T)$ to the empirical formula $A(T) = A_{BG} + (A(0) - A_{BG})[1 - (T/T_N)^\alpha]^\beta$.

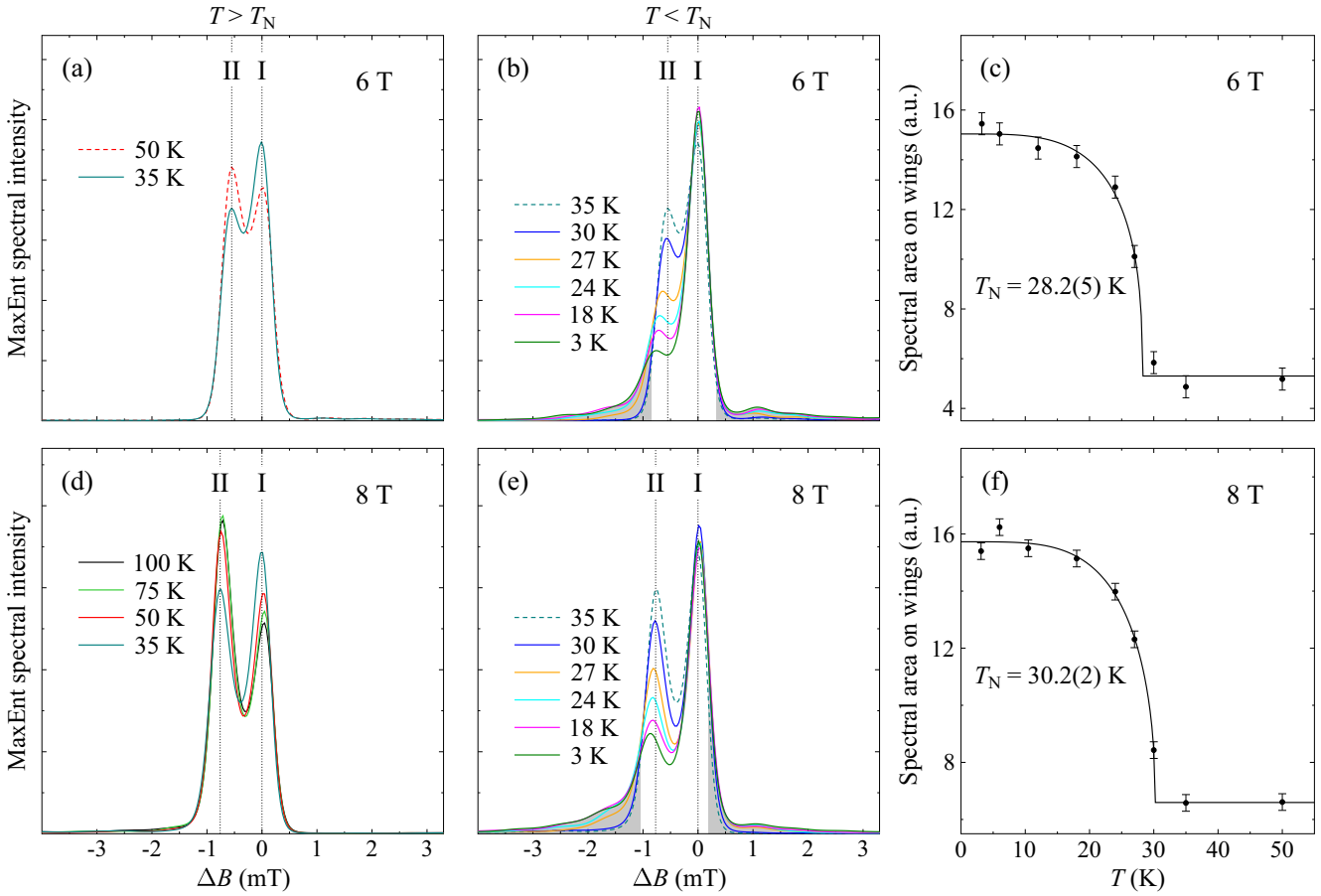

FIG. 8. High field TF-μSR spectra for κ-Cl. The central part of the spectrum is resolved into two distinct peaks labeled I and II. Spectra for a field of 6 T are shown (a) above and (b) below T_N. Grey shading in (b) indicates the outer spectral region whose area is plotted versus T in (c). [(d)–(f)] Comparable data for a field of 8 T.

2. Low field

Measurements made for the much lower TF of 0.45 T are shown in Fig. 9. In this case only a single peak is seen above T_N [Fig. 9(a)]. Below T_N some characteristic features appear [Fig. 9(b)]. The main peak becomes broader and reduced in amplitude and satellite peaks appear above and below the main peak, as was also seen in the higher field data. The T dependence of the area on the wings of the spectrum is shown in Fig. 9(c). At 0.45 T the broadening due to critical fluctuations is not as strongly suppressed as it was in the 6 T and 8 T data. In order to estimate T_N, we therefore fit the $T > T_N$ data points to a diverging critical fluctuation term scaling as $(T - T_N)^{-w}$, whereas the $T < T_N$ data points are again fitted to an order parameter term of the form $[1 - (T/T_N)^{\alpha}]^{\beta}$ This combined procedure gives an estimate of 22.7(4) K for T_N at 0.45 T [Fig. 9(c)].

3. Phase diagram for b-axis field orientation

The T_N values obtained from our data are compared with those from other techniques such as NMR and ZF-μSR in Fig. 10. From this figure it can be seen that all of the μSR and NMR data are consistent with a simple linear field dependence for T_N. Existing published magnetization data does not systematically cover this field range, so it is not clear whether the canted weak FM moment appears at a T_{wFM} that is simultaneous with T_N or else appears at a lower temperature. Thermal expansion studies [68] have shown a separation of these two temperatures at 8 T, with T_N at 28 K, similar to that seen by NMR and μSR, whereas a second feature that was found 5 K lower at 23 K was assigned to T_{wFM}. This same study however found a single transition in zero field at 28 K, which is not consistent with the magnetization and local field probe studies, which find that both transitions are at 23 K in zero field. Further temperature dependent magnetization studies should be able to clarify the evolution with field of the splitting between T_N and T_{wFM}.

4. Broad assignment of peaks I and II

A detailed analysis of the two central peaks of the high field data can also be made as the sum of two Gaussians and the results are plotted in Figs. 11 and 12. It can be seen again that peak I is barely affected by the transition whereas all of the parameters describing peak II change below the transition. Looking first at the peak positions [Figs. 11(a) and 12(a)], the peak shift ΔB for peak II above the transition is seen to approximately scale with the applied field (see right hand axes), reflecting b-axis moments produced by the bulk susceptibility for field applied along the b axis. This can contribute

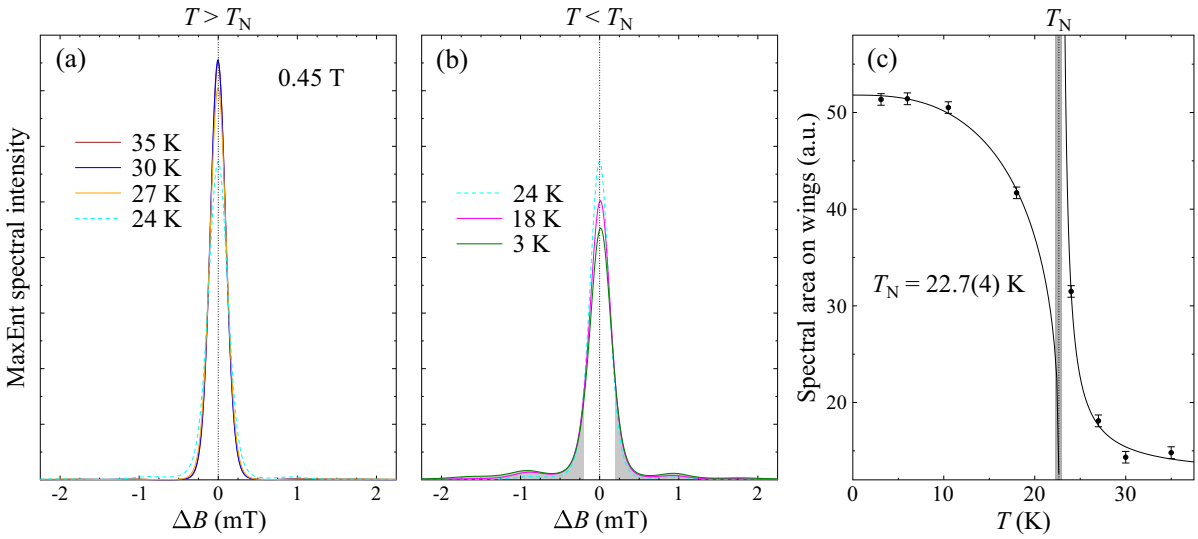

FIG. 9. Internal field spectra derived from MaxEnt analysis of TF μSR data on κ-Cl measured in a field of 0.45 T. (a) Spectra measured above T_N showing a single peak. (b) Spectra measured below T_N show the broadening and intensity reduction of the central peak with satellite peaks simultaneously appearing. The spectrum at 24 K, which is very close to T_N, is shown here as well for reference (dashed line). (c) The area of the outer spectral region plotted against temperature. Both critical broadening of the central peak and the appearance of satellite peaks contribute to this area. An estimate of T_N is obtained from a model that takes into account both of these effects.

an overall shift to the peak positions of a given site, which is tabulated in the final column of Table IV. The field shift there is made up of two terms, the first term is the dipolar field contribution and the second term describes the Lorentz field plus demagnetization field. The second term depends on the factor $N' = (3N - 1)/2$, where N is the demagnetization factor. Both N and N' are assumed to be close to 1 in the platelet geometry of the experiment. From the values obtained in the final column of Table IV with $N' = 1$, we expect the anion layer sites A1–A7 to show very little field shift, as the dipolar and Lorentz/demagnetization terms are closely canceling here, whereas the molecular layer sites all show a negative field shift when such b-axis moments are present. Thus we can make a broad assignment of the nonshifting peak I to anion sites and the shifting peak II to molecular sites. The temperature-dependent changes in relative amplitude of peaks I and II above T_N would then indicate changes in relative muon stopping probability between the molecular and anion layers, with stopping in the anion layer becoming a little less probable at higher T. Taking the sum of the peak I and peak II amplitudes compensates for this shift in site probabilities and allows the transition to be seen more clearly by following the behavior of the amplitude sum [Figs. 11(c) and 12(c)].

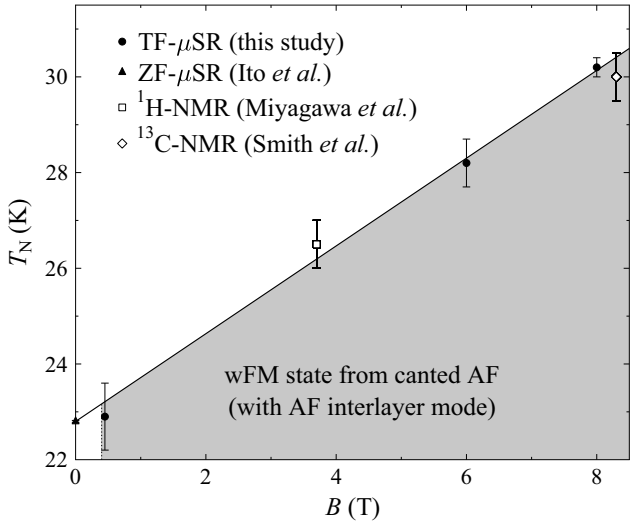

FIG. 10. T_N versus magnetic field B applied along b for κ-Cl. The $B = 0$ point is from low-field magnetization and ZF-μSR [25] and two different NMR studies [24,69] are included alongside the present TF-μSR results. All data points are seen to be consistent with a simple linear magnetic field dependence for T_N.

5. Site contributions to the TF spectrum

Whilst we have obtained a broad assignment of peaks I and II to the different types of site, we can go further in looking in more detail at the predicted splittings and shifts associated with the various sites in comparison with the TF data. This is done in Fig. 13 for the specific example of the 8 T spectrum measured at 3 K. A b-axis moment of 0.05 μ_B is found to be consistent with the observed splitting between the two central peaks. The plot uses the c-axis ordered moments we obtained earlier from analysis of the the ZF-μSR data, i.e., 0.36 μ_B for ET layer sites and 0.31 μ_B for anion layer sites. From Fig. 13 it can be seen that the broad satellite features are well reflected, along with the strong concentration of spectral weight in the two central peaks. The ratio of the 0.05 μ_B b-axis moment to the underlying 0.25 μ_B c-axis moment implies that at 8 T there is an overall field-induced spin canting of 11° towards the applied field direction.

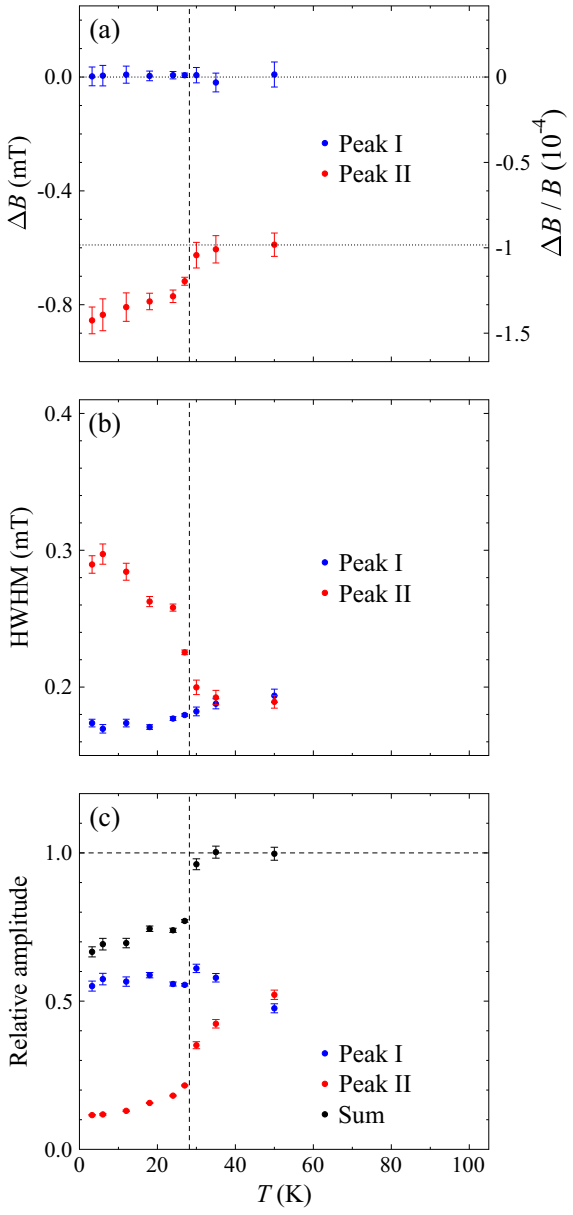

FIG. 11. (a) Shift, (b) width, and (c) relative amplitude of peaks I and II vs T for the 6-T data.

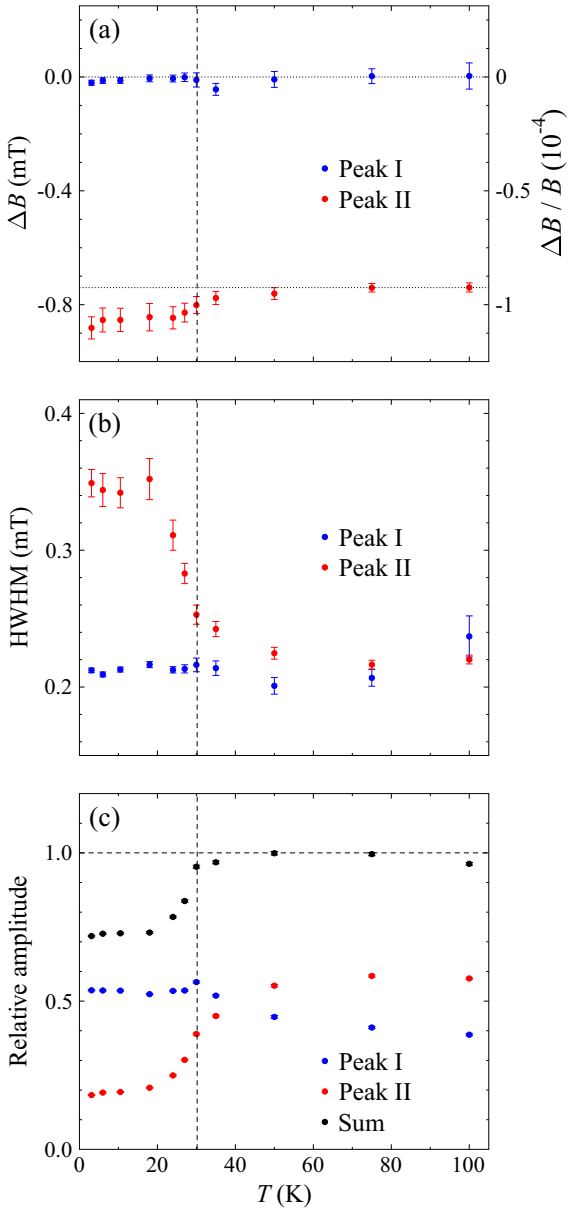

FIG. 12. (a) Shift, (b) width, and (c) relative amplitude of peaks I and II vs T for the 8-T data.

IV. CONCLUSIONS

This study has demonstrated how the incorporation of DFT+μ into μSR data analysis can enable a new quantitative approach to be made, which goes well beyond what was typically used before. This method is found to be viable even for quite a complex system, such as the κ-Cl system studied here, which has 236 atoms in its unit cell. We have shown that the same DFT-derived molecular spin distributions, when combined with dipolar field analysis, can be used to model both ^{1}H-NMR data and μSR data taken in ZF and TF configurations. This study has required the handling of large numbers of muon stopping sites and the methods developed here have now been incorporated into the the MuFinder program [70], which streamlines the processing of such sites.

We have found that an ordered moment of 0.25 μ_B aligned closely with the c axis describes the ^{1}H-NMR spectrum, whereas the ZF-μSR data indicates comparable but slightly higher values of 0.31 and 0.36 μ_B, dependent on the type of muon site. These moments are all significantly reduced from the value of $\sim$0.6 μ_B expected in the square lattice limit of the anisotropic Heisenberg triangular lattice, indicating that magnetic frustration is still relatively strong in κ-Cl, even though it is located in a region of the phase diagram with r ratio that is reduced far enough below 1 to lead to Néel ordering. Our studies are also able to confirm the nature of the metamagnetism of κ-Cl. We confirm that the magnetic coupling between moments in the two symmetry related layers in the crystal structure is intrinsically FM in nature, as previously deduced by Ishikawa *et al.* [37]. The application of a magnetic field above 0.4 T in the interlayer direction produces the

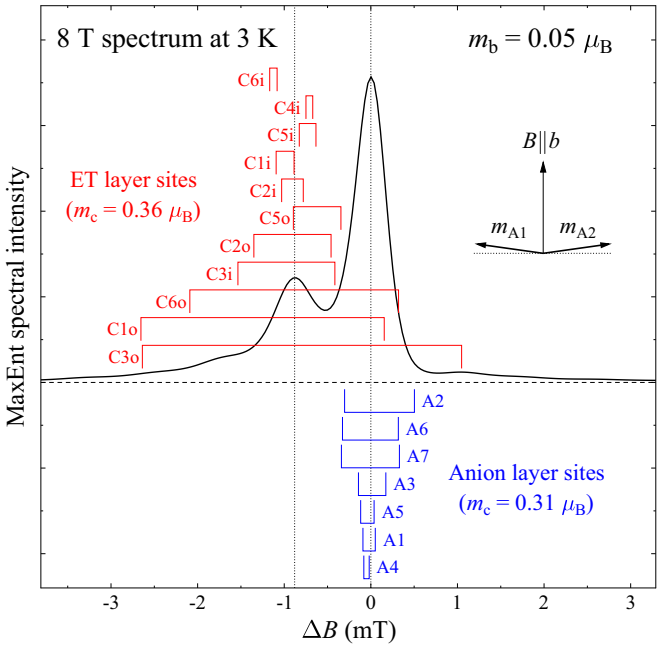

FIG. 13. The TF-μSR spectrum at 3 K in a field of 8 T compared with the peak positions predicted for moments in the ordered state of of 0.36 μ_B (ET layer sites) and 0.31 μ_B (anion layer sites). Each muon site site produces a pair of peaks as marked by the vertical lines and linked with a horizontal line. The splitting of the pair is proportional to m_c and the uniform shift of the pair is proportional to m_b. The constants of proportionality for the splitting and shift at each site given by the last two columns in Table IV. The predicted distribution of fields for $m_b = 0.05\ \mu_B$ is seen to give good consistency with the experimental spectrum. The inset illustrates the induced canting of the sublattices in one of the molecular layers.

metamagnetic transition by stabilizing the AF mode of coupling between the layers via the Zeeman energy associated with having weakly canted moments. These canted moments result from the presence of DM interactions, however the μSR spectra are not sensitive to the small canting angles produced by the DM interactions. At high fields, however, a field-induced moment along the field axis is clearly revealed in the TF-μSR spectrum via the shift of peak II relative to peak I. In the magnetically ordered phase this high field magnetization along the applied field direction is mainly due to field-induced canting of the transverse ordered moments from the c axis towards the b axis.

One key finding of our study is the contrasting behavior of the local fields for sites that are in different layers within the material, in particular the difference between stopping sites in the layers containing the spins, which are relatively sensitive to the magnetic state, and stopping sites in the layers that separate the spin-containing layers, which are relatively insensitive to the magnetic state. These conclusions should apply more generally beyond just the κ-$(ET)_2X$ family to a broader class of layered magnetic systems. Similar behavior would therefore be expected in muon studies of such systems whenever the muon stopping sites fall into distinct intralayer and interlayer categories with respect to the magnetic constituents.

In the specific case of κ-Cl, knowledge of the spin distribution over the ET dimer and possible stopping sites for the muons, combined with their spectral signatures in TF-μSR measurements extending to high fields, have allowed a detailed spectral analysis to be made. This information and the methodology we have developed will prove valuable in the further analysis of the properties of other members of the κ-$(ET)_2X$ family, particularly the QSL members, which will be the focus of further work.

Data associated with the paper will be made available via the Durham University data archive [71].

ACKNOWLEDGMENTS

Part of the work was carried out at the Swiss Muon Source, Paul Scherrer Institute, Switzerland and we are grateful for the provision of beamtime and experimental support. We acknowledge computing resources provided by Durham Hamilton HPC, the STFC Scientific Computing Department's SCARF cluster, and the UK National High Performance Computing Service ARCHER. The work was supported by EPSRC Grants No. EP/N024028/1, No. EP/N023803/1, and No. EP/N024486/1 and JSPS KAKENHI Grant No. 21K03438. B.M.H. thanks STFC for support via an ISIS Facility Development Studentship.

[1] L. Coleman, M. Cohen, D. Sandman, F. Yamagishi, A. Garito, and A. Heeger, Superconducting fluctuations and the Peierls instability in an organic solid, Solid State Commun. **12**, 1125 (1973).

[2] T. Mori and T. Kawamoto, Organic conductors–from fundamentals to nonlinear conductivity, Annu. Rep. Prog. Chem., Sect. C: Phys. Chem. **103**, 134 (2007).

[3] H. Mori, Materials viewpoint of organic superconductors, J. Phys. Soc. Jpn. **75**, 051003 (2006).

[4] N. P. Armitage, P. Fournier, and R. L. Greene, Progress and perspectives on electron-doped cuprates, Rev. Mod. Phys. **82**, 2421 (2010).

[5] J. Wosnitza, Spatially nonuniform superconductivity in quasi-two-dimensional organic charge-transfer salts, Crystals **8**, 183 (2018).

[6] C. C. Agosta, Inhomogeneous superconductivity in organic and related superconductors, Crystals **8**, 285 (2018).

[7] Y. Shimizu, K. Miyagawa, K. Kanoda, M. Maesato, and G. Saito, Spin Liquid State in an Organic Mott Insulator with a Triangular Lattice, Phys. Rev. Lett. **91**, 107001 (2003).

[8] K. Kanoda, Metal–insulator transition in κ-$(ET)_2X$ and $(DCNQI)_2M$: Two contrasting manifestation of electron correlation, J. Phys. Soc. Jpn. **75**, 051007 (2006).

[9] B. J. Powell and R. H. McKenzie, Quantum frustration in organic Mott insulators: From spin liquids to unconventional superconductors, Rep. Prog. Phys. **74**, 056501 (2011).

[10] H.-Y. Yang, A. M. Läuchli, F. Mila, and K. P. Schmidt, Effective Spin Model for the Spin-Liquid Phase of the Hubbard Model on the Triangular Lattice, Phys. Rev. Lett. **105**, 267204 (2010).

[11] T. Yoshioka, A. Koga, and N. Kawakami, Quantum Phase Transitions in the Hubbard Model on a Triangular Lattice, Phys. Rev. Lett. **103**, 036401 (2009).

[12] B. Kyung and A. M. S. Tremblay, Mott Transition, Antiferromagnetism, and D-Wave Superconductivity in Two-Dimensional Organic Conductors, Phys. Rev. Lett. **97**, 046402 (2006).

[13] H. C. Kandpal, I. Opahle, Y.-Z. Zhang, H. O. Jeschke, and R. Valenti, Revision of Model Parameters for κ-Type Charge Transfer Salts: An *Ab Initio* Study, Phys. Rev. Lett. **103**, 067004 (2009).

[14] T. Koretsune and C. Hotta, Evaluating model parameters of the κ- and β'-type Mott insulating organic solids, Phys. Rev. B **89**, 045102 (2014).

[15] T. Hiramatsu, Y. Yoshida, G. Saito, A. Otsuka, H. Yamochi, M. Maesato, Y. Shimizu, H. Ito, and H. Kishida, Quantum spin liquid: Design of a quantum spin liquid next to a superconducting state based on a dimer-type ET Mott insulator, J. Mater. Chem. C **3**, 1378 (2015).

[16] S. J. Blundell, R. De Renzi, T. Lancaster, and F. L. Pratt, eds., *Muon Spectroscopy - An Introduction* (Oxford University Press, Oxford, 2021).

[17] F. L. Pratt, Superconductivity and magnetism in organic materials studied with μSR, J. Phys. Soc. Jpn. **85**, 091008 (2016).

[18] T. Hiramatsu, Y. Yoshida, G. Saito, A. Otsuka, H. Yamochi, M. Maesato, Y. Shimizu, H. Ito, Y. Nakamura, H. Kishida *et al.*, Design and preparation of a quantum spin liquid candidate κ-$(ET)_2Ag_2(CN)_3$ having a nearby superconductivity, Bull. Chem. Soc. Jpn. **90**, 1073 (2017).

[19] H. O. Jeschke, M. de Souza, R. Valentí, R. S. Manna, M. Lang, and J. A. Schlueter, Temperature dependence of structural and electronic properties of the spin-liquid candidate κ-(BEDT-TTF)$_2$Cu$_2$(CN)$_3$, Phys. Rev. B **85**, 035125 (2012).

[20] F. L. Pratt, P. J. Baker, S. J. Blundell, T. Lancaster, S. Ohira-Kawamura, C. Baines, Y. Shimizu, K. Kanoda, I. Watanabe, and G. Saito, Magnetic and non-magnetic phases of a quantum spin liquid, Nature (London) **471**, 612 (2011).

[21] N. Hassan, S. Cunningham, M. Mourigal, E. I. Zhilyaeva, S. A. Torunova, R. N. Lyubovskaya, J. A. Schlueter, and N. Drichko, Evidence for a quantum dipole liquid state in an organic quasi–two-dimensional material, Science **360**, 1101 (2018).

[22] C. Hotta, Quantum electric dipoles in spin-liquid dimer Mott insulator κ-$ET_2Cu_2(CN)_3$, Phys. Rev. B **82**, 241104(R) (2010).

[23] M. Naka and S. Ishihara, Quantum melting of magnetic order in an organic dimer Mott-insulating system, Phys. Rev. B **93**, 195114 (2016).

[24] K. Miyagawa, A. Kawamoto, Y. Nakazawa, and K. Kanoda, Antiferromagnetic Ordering and Spin Structure in the Organic Conductor, κ-(BEDT-TTF)$_2$Cu[N(CN)$_2$]Cl, Phys. Rev. Lett. **75**, 1174 (1995).

[25] M. Ito, T. Uehara, H. Taniguchi, K. Satoh, Y. Ishii, and I. Watanabe, Zero-field magnetism of a two-dimensional antiferromagnet, κ-(BEDT-TTF)$_2$Cu[N(CN)$_2$]Cl, determined by muon spin rotation and magnetization measurements, J. Phys. Soc. Jpn. **84**, 053703 (2015).

[26] T. Ishiguro, K. Yamaji, and G. Saito, *Organic Superconductors*, 2nd ed. (Springer, Berlin, 1997).

[27] T. Mori, A. Kobayashi, Y. Sasaki, H. Kobayashi, G. Saito, and H. Inokuchi, Band structures of two types of (BEDT-TTF)$_2$I$_3$, Bull. Chem. Soc. Jpn. **57**, 627 (1984).

[28] M. J. Frisch, G. W. Trucks, H. B. Schlegel, G. E. Scuseria, M. A. Robb, J. R. Cheeseman, G. Scalmani, V. Barone, G. A. Petersson, H. Nakatsuji *et al.*, Gaussian 16 Revision B.01, Gaussian Inc. Wallingford, CT (2016).

[29] A. D. Becke, Density-functional thermochemistry. III. The role of exact exchange, J. Chem. Phys. **98**, 5648 (1993).

[30] C. Lee, W. Yang, and R. G. Parr, Development of the Colle-Salvetti correlation-energy formula into a functional of the electron density, Phys. Rev. B **37**, 785 (1988).

[31] T. H. Dunning, Gaussian basis sets for use in correlated molecular calculations. I. The atoms boron through neon and hydrogen, J. Chem. Phys. **90**, 1007 (1989).

[32] U. Welp, S. Fleshler, W. K. Kwok, G. W. Crabtree, K. D. Carlson, H. H. Wang, U. Geiser, J. M. Williams, and V. M. Hitsman, Weak Ferromagnetism in κ-$(ET)_2Cu[N(CN)_2]Cl$, Where (ET) is Bis(Ethylenedithio)Tetrathiafulvalene, Phys. Rev. Lett. **69**, 840 (1992).

[33] M. Pinterić, M. Miljak, N. Biškup, O. Milat, I. Aviani, S. Tomić, D. Schweitzer, W. Strunz, and I. Heinen, Magnetic anisotropy and low-frequency dielectric response of weak ferromagnetic phase in κ-(BEDT-TTF)$_2$Cu[N(CN)$_2$]Cl, where BEDT-TTF is Bis(ethylenedithio)tetrathiafulvalene, Eur. Phys. J. B **11**, 217 (1999).

[34] I. Dzyaloshinsky, A thermodynamic theory of "weak" ferromagnetism of antiferromagnetics, J. Phys. Chem. Solids **4**, 241 (1958).

[35] T. Moriya, Anisotropic superexchange interaction and weak ferromagnetism, Phys. Rev. **120**, 91 (1960).

[36] D. F. Smith, C. P. Slichter, J. A. Schlueter, A. M. Kini, and R. G. Daugherty, Precise Determination of the Orientation of the Dzialoshinskii-Moriya Vector in $\kappa-$(BEDT-TTF)$_2$Cu[N(CN)$_2$]Cl, Phys. Rev. Lett. **93**, 167002 (2004).

[37] R. Ishikawa, H. Tsunakawa, K. Oinuma, S. Michimura, H. Taniguchi, K. Satoh, Y. Ishii, and H. Okamoto, Zero-field spin structure and spin reorientations in layered organic antiferromagnet, κ-(BEDT-TTF)$_2$Cu[N(CN)$_2$]Cl, with Dzyaloshinskii-Moriya interaction, J. Phys. Soc. Jpn. **87**, 064701 (2018).

[38] S. M. Winter, K. Riedl, and R. Valentí, Importance of spin-orbit coupling in layered organic salts, Phys. Rev. B **95**, 060404(R) (2017).

[39] F. Kagawa, Y. Kurosaki, K. Miyagawa, and K. Kanoda, Field-induced staggered magnetic moment in the quasi-two-dimensional organic Mott insulator $\kappa-$(BEDT-TTF)$_2$Cu[N(CN)$_2$]Cl, Phys. Rev. B **78**, 184402 (2008).

[40] F. L. Pratt, Dipolar field calculations for muon spectroscopy (2019), https://doi.org/10.5281/zenodo.3476167.

[41] B. Schmidt, M. Siahatgar, and P. Thalmeier, Ordered moment in the anisotropic and frustrated square lattice Heisenberg model, Phys. Rev. B **83**, 075123 (2011).

[42] B. M. Huddart, M. Gomilšek, T. J. Hicken, F. L. Pratt, S. J. Blundell, P. A. Goddard, S. J. Kaech, J. L. Manson, and T. Lancaster, Magnetic order and ballistic spin transport in a sine-Gordon spin chain, Phys. Rev. B **103**, L060405 (2021),.

[43] T. Lancaster, F. Xiao, B. M. Huddart, R. C. Williams, F. L. Pratt, S. J. Blundell, S. J. Clark, R. Scheuermann, T. Goko, S. Ward *et al.*, Quantum magnetism in molecular spin ladders probed with muon-spin spectroscopy, New J. Phys. **20**, 103002 (2018).

[44] S. J. Blundell, J. S. Möller, T. Lancaster, P. J. Baker, F. L. Pratt, G. Seber, and P. M. Lahti, μSR study of magnetic order in the organic quasi-one-dimensional ferromagnet F4BImNN, Phys. Rev. B **88**, 064423 (2013).

[45] S. J. Clark, M. D. Segall, C. J. Pickard, P. J. Hasnip, M. J. Probert, K. Refson, and M. Payne, First principles methods using CASTEP, Z. Kristallogr. **220**, 567 (2005).

[46] J. P. Perdew, K. Burke, and M. Ernzerhof, Generalized Gradient Approximation Made Simple, Phys. Rev. Lett. **77**, 3865 (1996).

[47] H. J. Monkhorst and J. D. Pack, Special points for Brillouin-zone integrations, Phys. Rev. B **13**, 5188 (1976).

[48] A. Tkatchenko and M. Scheffler, Accurate Molecular van Der Waals Interactions from Ground-State Electron Density and Free-Atom Reference Data, Phys. Rev. Lett. **102**, 073005 (2009).

[49] M. Pinterić, D. Rivas Góngora, Ž. Rapljenović, T. Ivek, M. Čulo, B. Korin-Hamzić, O. Milat, B. Gumhalter, P. Lazić, M. Sanz Alonso *et al.*, Electrodynamics in organic dimer insulators close to Mott critical point, Crystals **8**, 190 (2018).

[50] L. Liborio, S. Sturniolo, and D. Jochym, Computational prediction of muon stopping sites using ab initio random structure searching (AIRSS), J. Chem. Phys. **148**, 134114 (2018).

[51] B. D. Rainford and G. J. Daniell, μSR frequency spectra using the maximum entropy method, Hyperfine Interact. **87**, 1129 (1994).

[52] F. L. Pratt, WIMDA: A muon data analysis program for the Windows PC, Phys. B: Condens. Matter **289-290**, 710 (2000).

[53] S. J. Blundell, P. A. Pattenden, F. L. Pratt, R. M. Valladares, T. Sugano, and W. Hayes, μ^+SR of the organic ferromagnet *p*-NPNN: Diamagnetic and paramagnetic states, Europhys. Lett. **31**, 573 (1995).

[54] M. Heming, E. Roduner, B. D. Patterson, W. Odermatt, J. Schneider, H. Baumeler, H. Keller, and I. M. Savic, Detection of muonated free radicals through the effects of avoided level crossing. Theory and analysis of spectra, Chem. Phys. Lett. **128**, 100 (1986).

[55] R. F. Kiefl, S. Kreitzman, M. Celio, R. Keitel, G. M. Luke, J. H. Brewer, D. R. Noakes, P. W. Percival, T. Matsuzaki, and K. Nishiyama, Resolved nuclear hyperfine structure of a muonated free radical using level-crossing spectroscopy, Phys. Rev. A **34**, 681 (1986).

[56] S. J. Blundell, Muon-spin rotation studies of electronic properties of molecular conductors and superconductors, Chem. Rev. **104**, 5717 (2004).

[57] F. L. Pratt, S. J. Blundell, T. Jestädt, B. W. Lovett, R. M. Macrae, and W. Hayes, Muon radical states in some electron donor and acceptor molecules, Magn. Reson. Chem. **38**, S27 (2000).

[58] R. M. Macrae, Free radical probes of organic conductor constituents: Electronic structures and hyperfine properties, Magn. Reson. Chem. **38**, S33 (2000).

[59] M. Dumm, D. Faltermeier, N. Drichko, M. Dressel, C. Meziere, and P. Batail, Bandwidth-controlled Mott transition in κ-(BEDT-TTF)$_2$Cu[N(CN)$_2$]Br$_x$Cl$_{1-x}$: Optical studies of correlated carriers, Phys. Rev. B **79**, 195106 (2009).

[60] J. Ferber, K. Foyevtsova, H. O. Jeschke, and R. Valenti, Unveiling the microscopic nature of correlated organic conductors: The case of κ-(ET)$_2$Cu[N(CN)$_2$]Br$_x$Cl$_{1-x}$, Phys. Rev. B **89**, 205106 (2014).

[61] P. Hauke, Quantum disorder in the spatially completely anisotropic triangular lattice, Phys. Rev. B **87**, 014415 (2013).

[62] Y. Yamauchi, M. V. Kartsovnik, T. Ishiguro, M. Kubota, and G. Saito, Angle-dependent magnetoresistance and Shubnikov-de Haas oscillations in the organic superconductor κ-(BEDT-TTF)$_2$Cu[N(CN)$_2$]Cl under pressure, J. Phys. Soc. Jpn. **65**, 354 (1996).

[63] F. L. Pratt, Using Shubnikov-de Haas data to estimate the magnetic frustration parameter t'/t in the spin-liquid system κ-ET$_2$Cu$_2$(CN)$_3$, Phys. B: Condens. Matter **405**, S205 (2010).

[64] S. L. Lee, F. L. Pratt, S. J. Blundell, C. M. Aegerter, P. A. Pattenden, K. H. Chow, E. M. Forgan, T. Sasaki, W. Hayes, and H. Keller, Investigation of Vortex Behavior in the Organic Superconductor κ-(BEDT-TTF)$_2$Cu(SCN)$_2$ Using Muon Spin Rotation, Phys. Rev. Lett. **79**, 1563 (1997).

[65] S. J. Blundell, S. L. Lee, F. L. Pratt, C. M. Aegerter, T. Jestädt, B. W. Lovett, C. Ager, T. Sasaki, V. N. Laukhin, E. Laukhina *et al.*, Stability of the vortex lattice in ET superconductors studied by μSR, Synth. Met. **103**, 1925 (1999).

[66] F. L. Pratt, S. J. Blundell, A. Husmann, I. M. Marshall, B. W. Lovett, W. Hayes, S. L. Lee, C. Ager, F. Y Ogrin, T. Sasaki *et al.*, BEDT-TTF superconductors studied by μSR, Phys. B: Condens. Matter **289-290**, 396 (2000).

[67] T. Lancaster, S. J. Blundell, F. L. Pratt, and J. A. Schlueter, Superconductivity and fluctuating magnetism in quasi-two-dimensional κ-(BEDT-TTF)$_2$Cu[N(CN)$_2$]Br probed with implanted muons, Phys. Rev. B **83**, 024504 (2011).

[68] P. Lunkenheimer, J. Müller, S. Krohns, F. Schrettle, A. Loidl, B. Hartmann, R. Rommel, M. de Souza, C. Hotta, J. A. Schlueter, and M. Lang, Multiferroicity in an organic charge-transfer salt that is suggestive of electric-dipole-driven magnetism, Nat. Mater. **11**, 755 (2012).

[69] D. F. Smith, S. M. De Soto, C. P. Slichter, J. A. Schlueter, A. M. Kini, and R. G. Daugherty, Dzialoshinskii-Moriya interaction in the organic superconductor κ-(BEDT-TTF)$_2$Cu[N(CN)$_2$]Cl, Phys. Rev. B **68**, 024512 (2003).

[70] B. M. Huddart, A. Hernández-Melián, T. J. Hicken, M. Gomilšek, Z. Hawkhead, S. J. Clark, F. L. Pratt, and T. Lancaster, MuFinder: A program to determine and analyse muon stopping sites, Comput. Phys. Commun. **280**, 108488 (2022).

[71] Data available at https://doi.org/10.15128/r26w924b87p.